Dalton Transactions

RSCPublishing

PAPER

View Article Online
View Journal | View Issue

Cite this: *Dalton Trans.*, 2013, **42**, 1550

A new layered triangular antiferromagnet Li_4FeSbO_6: spin order, field-induced transitions and anomalous critical behavior†

E. A. Zvereva,*[a,b] O. A. Savelieva,[a] Ya. D. Titov,[a] M. A. Evstigneeva,[c] V. B. Nalbandyan,[c] C. N. Kao,[d] J.-Y. Lin,[d] I. A. Presniakov,[e] A. V. Sobolev,[e] S. A. Ibragimov,[e] M. Abdel-Hafiez,[b] Yu. Krupskaya,[b] C. Jähne,[f] G. Tan,[f] R. Klingeler,[f] B. Büchner[b] and A. N. Vasiliev[a]

Structure, electrochemical, magnetic and resonance properties of new layered antimonate Li_4FeSbO_6 were comprehensively studied using powder X-ray diffraction, cyclic voltammetry, magnetic susceptibility, heat capacity, electron spin resonance and Mössbauer spectroscopy. In the crystal structure the iron ions form the triangular network within $(LiFeSbO_6)^{3-}$ layers alternating with nonmagnetic lithium layers. The electrochemical activity studied implies an Fe^{3+}/Fe^{4+} redox couple at 4.3 V (ox.) and 3.9 V (red.) thereby revealing that Li can be reversibly extracted. The long-range antiferromagnetic order was found to occur at the Néel temperature, $T_N \approx 3.6$ K, confirmed both by the magnetic susceptibility data and specific heat ones. The effective magnetic moment is estimated to be 5.93 μ_B/f.u. and satisfactorily agrees with theoretical estimations assuming high-spin configuration of Fe^{3+} ($S = 5/2$). In the magnetically ordered state, though, the magnetization demonstrates rather peculiar behavior. An additional anomaly on the $M(T)$ curves appears at $T_2 < T_N$ in moderate magnetic field. The positions of transitions at T_N and T_2 separate increasingly with increasing external field. Multiple measurements consistently demonstrated field-sensitive moving of magnetic phase boundaries constituting a unique phase diagram for the compound under study. The complex low-dimensional (2D) nature of magnetic coupling was confirmed by the dynamic magnetic properties study. Electron spin resonance from Fe^{3+} ions in paramagnetic phase is characterized by a temperature independent effective g-factor of 1.99 ± 0.01. However, the distortion and broadening of the ESR line were found to take place upon approaching the magnetically ordered state from above. The divergence of the temperature-dependent linewidth is analyzed in terms of both critical behavior close to long-range magnetic order and the Berezinskii–Kosterlitz–Thouless (BKT)-type transition. Heat capacity measurements even at zero field manifested an appearance of the additional anomaly at temperatures below the Néel temperature. The temperature dependence of ESR intensity, linewidth and shift of the resonant field imply an extended region of short-range order correlations in the compound studied. The rich variety of the anomalies in magnetic and resonance properties makes this new antimonate a very interesting system to investigate the multiple phase transitions and competing exchange interaction due to the critical role of the layered structure organization accompanied by the frustration effects in triangular antiferromagnets.

Received 24th August 2012,
Accepted 18th October 2012

DOI: 10.1039/c2dt31938a

www.rsc.org/dalton

Introduction

Currently, the investigation of layered oxides of alkali and transition metals is one of the most active areas of materials science. The attention is due to both the discovery of a great variety of ground states in the quasi-two-dimensional (2D) systems and hopes for the utilization of the oxides with alkali metals in electrochemical power devices. In many cases, magnetism in these compounds has quasi-two-dimensional (2D) character due to weak interlayer coupling between the

---

[a] *Faculty of Physics, Moscow State University, 119991 Moscow, Russia. E-mail: zvereva@mig.phys.msu.ru; Fax: +7 495 932 9217; Tel: +7 495 939 4811*
[b] *Leibniz Institute for Solid State and Materials Research IFW Dresden, D-01069, Germany*
[c] *Chemistry Faculty, Southern Federal University, Rostov-on-Don 344090, Russia*
[d] *Institute of Physics, National Chiao Tung University, Hsinchu 30010, Taiwan*
[e] *Chemistry Faculty, Moscow State University, 119991 Moscow, Russia*
[f] *Kirchhoff Institute for Physics, University of Heidelberg, D-69120 Heidelberg, Germany*

† Electronic supplementary information (ESI) available. See DOI: 10.1039/c2dt31938a

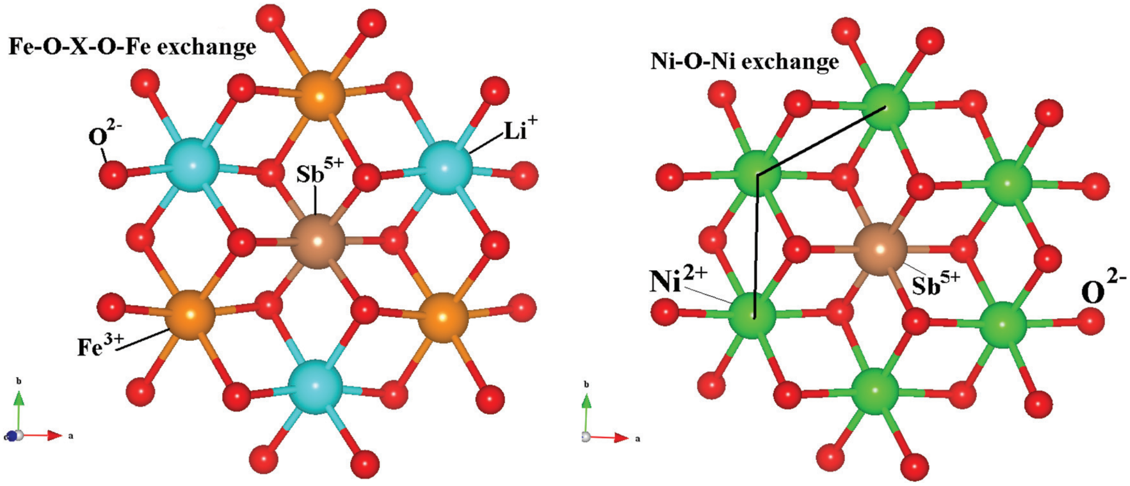

Fig. 1 Magnetoactive layers: proposed local cation ordering in Li_4FeSbO_6 forming a triangular net of magnetic Fe^{3+} ions (left) and a honeycomb net of magnetic Ni^{2+} ions in structurally related $Li_3Ni_2SbO_6$ [30] (right).

magnetically active layers separated in the crystal structure by non-magnetic layers of the alkali ions. In general, the reduced dimensionality and the interplay between spin, orbital and charge degrees of freedom yield a variety of fascinating phenomena like superconductivity, multiferroicity, quantum liquid and spin gap states, chiral phases, *etc.* Among the quasi-2D systems, the triangular lattice antiferromagnets (TLAFM) are especially interesting since the triangular geometry of a magnetic cation's ordering results in special competition between forces that can frustrate primary interactions and therefore often allows weaker and longer range interactions to dominate magnetic behavior.[1–17]

The data on actually realized phases in the quantum quasi-2D TLAFM are still controversial.[18–21] From the experimental viewpoint, many intriguing effects have been found in the quasi-2D TLAFM or related lattice compounds. In particular, for $LiNiO_2$,[2] $NaTiO_2$,[3] $SrCr_{9p}Ga_{12-9p}O_{19}$,[4] $Cu_{1-x}Ag_xCrO_2$ [5] and $NiGa_2S_4$,[6] spin-liquid behaviors such as many-body singlet excitations were observed. In the metallic quasi-2D triangular lattice Na cobaltates Na_xCoO_2 and $Na_xCoO_2{\cdot}yH_2O$, furthermore, an anomalously large thermoelectric response[7,8] and superconductivity[9] were found. The $CuCrO_2$ and $AgCrO_2$ compounds exhibit multiferroic behavior, the coexistence of magnetic order and ferroelectricity, concomitantly with a 120° spin-spiral structure.[10,11] A spectacular example of multiferroic behavior due to the TLAFM environment was also found in the layered molybdate $RbFe(MoO_4)_2$.[12–14] For its isostructural analogue $KFe(MoO_4)_2$ with a distorted triangular lattice, the coexisting chiral and collinear phases have been claimed.[15] $CuFeO_2$ has shown the successive magnetic phase transitions (from paramagnetic to partially disordered and eventually to a four-sublattice ground state) characterized by the quasi-Ising character in contrast to the non-collinear three-sublattice 120° magnetic structure expected for a typical Heisenberg spin TLAFM.[16,17] Unusual spin relaxation has been observed in the 2D frustrated TLAFM[22,23] and ascribed to the so-called magnetic vortices. Formation of these topological defects due to short-range spin correlations giving rise to an additional degree of freedom called the vector chirality, *i.e.*, left- or right-handed circulation, has been theoretically predicted for 2D AFM by Kosterlitz and Thouless and independently by Berezinskii.[24–27]

In contrast to the compounds mentioned above, the properties of the antimonates and tellurates of alkali and transition metals are largely unexplored at present. Structurally, the honeycomb crystal structure, which is a variant of triangular geometry, occurs frequently in these oxides.[28–38] The frustration that arises from the presence of strong competition between nearest neighbor and second nearest neighbor magnetic interactions may lead to nontrivial types of magnetic ordering at low temperatures similarly to TLAFM. Indeed, while $Li_3Ni_2SbO_6$,[30] $Na_3Co_2SbO_6$ and $Na_2Co_2TeO_6$ [31] exhibit AFM long-range order, structurally related $Na_3Cu_2SbO_6$ [32–34,38] was found to have a singlet ground state with spin gap behavior and was best defined recently as a short-range AF–F one-dimensional (1D) alternate chain model.[38]

The focus of the present article is synthesis and comprehensive study of a new layered antimonate Li_4FeSbO_6, which was found to be structurally similar to the recently studied honeycomb compound $Li_3Ni_2SbO_6$.[30] In contrast to the latter though, a honeycomb-type cell in Li_4FeSbO_6 contains two times less magnetic ions (Fe^{3+}) in an octahedral oxygen environment (Fig. 1), that results in formation of the triangular magnetic net in which spins $S = 5/2$ are coupled through longer antiferromagnetic superexchange interactions involving a nonmagnetic Li/Sb cation and two oxygen anions.

Experimental

Li_4FeSbO_6 was prepared by conventional solid-state reactions using reagent-grade Li_2CO_3, Fe_2O_3 and $Sb_2O_5{\cdot}2.74H_2O$. $FeSbO_4$ was synthesized first, verified by powder X-ray diffraction (XRD), and then mixed thoroughly with lithium carbonate in a

1 : 2 molar ratio. The mixture was pressed, calcined for 30 min at 1020 K, 30 min at 1070 K, and 3 hours at 1320 K with intermediate regrinding, pressing and final quenching. At the final heating stage, the pellets were embedded into the powder of the same compositions and the crucible was covered in order to avoid compositional changes due to volatilization.

XRD studies were performed with an ARL X'TRA diffractometer equipped with a solid-state Si(Li) detector set to measure pure CuK_α radiation, thus eliminating Fe fluorescence, CuK_β and polychromatic background. Structural analysis was done by the Rietveld method using the GSAS+EXPGUI program suite.[39,40] The obtained powder pattern was submitted for inclusion into the Powder Diffraction File®.

The ^{57}Fe Mössbauer spectra were recorded at 10–300 K using a conventional constant-acceleration spectrometer. The radiation source ^{57}Co(Rh) was kept at room temperature. All isomer shifts refer to the α-Fe absorber at 300 K. The experimental spectra were processed and analyzed using methods of spectral simulation and reconstruction for the distribution functions of hyperfine parameters corresponding to the partial spectra implemented in the MSTools program package.[41]

The electrochemical activity was studied in a Swagelock-type cell.[42] For the electrode, 75 wt% synthesized powder, 20 wt% Carbon Black (Timcal, Switzerland), and 5 wt% of polyvinylidene fluoride (PVDF) binder (Solexis, Tavaux Cedex, France) were mixed and soaked with anhydrous 1-methyl-2-pyrrolidinone (NMP, Sigma-Aldrich, 99%). 12 mg of the resulting slurry was pasted on a 10 mm diameter Al-mesh, dried overnight at 100 °C and pressed. After additional drying in a vacuum for 24 h at 100 °C, the two-electrode Swagelok-like cell was assembled in an Ar-atmosphere glove box (O_2/H_2O < 2 ppm). The negative lithium-metal electrode was mounted on a zinc current collector and separated from the counter electrode by electrolyte soaked Whatman borosilicate glass fibres, with a 1 M $LiPF_6$ salt solution in ethylene carbonate (EC)/dimethyl carbonate (DMC) mixture 1 : 1 (Merck) as the electrolyte. Cyclic voltammetry between 2.9 V and 4.6 V with a sweeping rate of 0.1 mV s^{-1} was performed in a climate chamber at 25 °C using a VMP3 multichannel potentiostate (BIO-Logic SAS, France).[42]

Magnetic measurements were performed by means of a Quantum Design SQUID-VSM magnetometer. The temperature dependence of the magnetic susceptibility was measured under variation of the magnetic field up to $B = 7$ T in the temperature range 1.8–300 K. In addition, the isothermal magnetization curves were obtained in external fields up to 7 T at various constant temperatures (T = 1.8, 2, 2.5, 3, 3.8, 5, 8, 12, 20 K) after cooling the sample in zero magnetic field.

Heat capacity measurements were carried out by a relaxation method using a Quantum Design PPMS system. The plate-shaped sample of ≈0.2 mm thickness and 2.66 mg mass was obtained by compressing the polycrystalline powder. Data were collected at zero magnetic field and under applied fields up to 9 T in the temperature range 0.5–300 K.

Low-frequency electron spin resonance (ESR) studies were carried out using an X-band ESR spectrometer CMS 8400 (ADANI) ($f \approx 9.4$ GHz, $B \leq 0.7$ T) equipped with a low temperature mount, operating in the range T = 5–470 K. The effective g-factors of our samples have been calculated with respect to a BDPA (*a*,*g*-bisdiphenyline-*b*-phenylallyl) reference sample with g_{et} = 2.00359. High-field/high-frequency electron spin resonance (HF-ESR) measurements were performed using a home made spectrometer based on a Millimeterwave Vector Network Analyzer (AB Millimetré).[43] In the high-frequency regime (f = 83–332 GHz), the transmission of the microwave radiation through the Li_4FeSbO_6 sample (in the form of the plate compressed from the powder) was measured as a function of magnetic field without a resonance cavity.

Results and discussion

Powder XRD study

The XRD pattern of the new compound (Fig. 2) is very similar to those of other superlattices derived from the α-$NaFeO_2$ structure type, such as Na_2IrO_3,[35] Na_4FeSbO_6,[36] $Na_3M_2SbO_6$ (M = Co, Ni, Zn, Mg)[37] and $Li_3Ni_2SbO_6$.[30] There are sharp peaks corresponding to the rhombohedral subcell of the α-$NaFeO_2$ type and diffuse superlattice reflections due to a 1 : 2 (or 1 : 1 : 1) cation ordering within octahedral layers. Usually, these patterns permit indexing in both trigonal and monoclinic systems, with space groups $P3_112$ and $C2/m$ (or $C2/c$), respectively.[28,30,36,37] In the case of Li_4FeSbO_6, however, the trigonal variant was definitely giving a worse solution and monoclinic setting was preferred. No extra reflections from foreign phases were observed at the 0.2% detection limit.

The initial structural model, $C2/m$, was based on that of $Li_3Ni_2SbO_6$,[30] with $Li_{1/2}Fe_{1/2}$ substituting for Ni. Then, partial Li/Fe ordering was supposed. To enable this, the mirror plane of the space group $C2/m$ was eliminated and the four-fold Ni site was split into two independent sites with starting Li/Fe occupancies of 0.3/0.7 and 0.7/03 in the space group $C2$. This resulted in much larger discrepancy factors; refinement of the

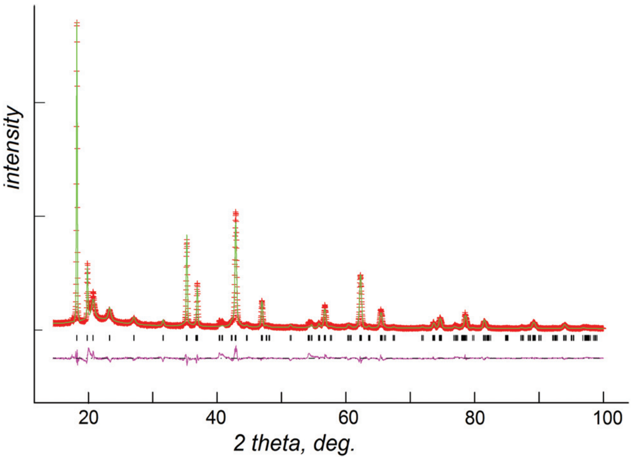

Fig. 2 XRD powder pattern of Li_4FeSbO_6 taken with CuK_α radiation. Crosses, experimental data; green line, calculated profile; violet line below, difference profile; vertical bars, Bragg positions.

Table 1 Powder XRD structural data for Li_4FeSbO_6

Space group	C 1 2/m 1 (12) – monoclinic
Cell	a = 5.1706(5) Å, b = 8.9382(5) Å, c = 5.1635(2) Å, β = 109.49(1)°, V = 224.96(48) Å^3, Z = 2
Refinement data	λ = 1.5406 Å, R_p = 0.103, wR_p = 0.146, χ^2 = 6.33

Atomic parameters

Atom	Wyck.	S.O.F.	x/a	y/b	z/c	U (Å^2)
Sb1	2a	0.759(4)	0	0	0	0.0378(3)
Fe1	2a	0.241(4)	0	0	0	0.0378(3)
Fe2	4g	0.380(2)	0	0.3383(3)	0	0.003(2)
Li1	4g	0.5	0	0.3383(3)	0	0.003(2)
Sb2	4g	0.120(2)	0	0.3383(3)	0	0.003(2)
Li2	4h		0	0.14817(4)	0.5	0.0284(5)
Li3	2d		0	0.5	0.5	0.0354(8)
O1	4i		0.7965(3)	0	0.2245(3)	0.014(2)
O2	8j		0.2192(2)	0.14990(10)	0.2320(2)	0.0016(12)

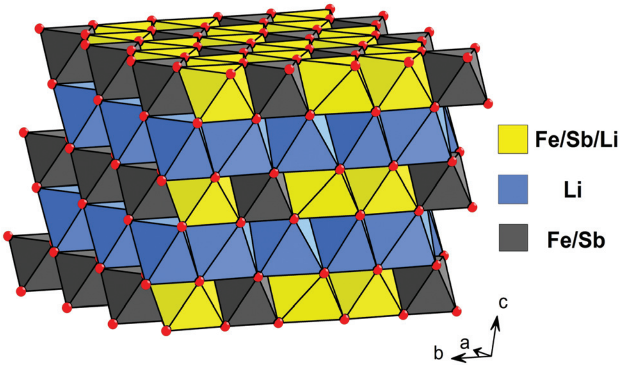

Fig. 3 Polyhedral presentation of the Li_4FeSbO_6 crystal structure. Note that mixed site occupancies are largely fictitious, as discussed in the text.

Li/Fe occupancies converged to essentially identical values for both sites. Therefore, the initial $C2/m$ model was preferred. At this stage, an elevated thermal parameter for Sb and a reduced thermal parameter for Fe/Li were noticed suggesting possible Fe/Sb inversion, and the inversion rate was refined to be 24%.

Refinement results are listed in Table 1 and a polyhedral view of the structure is shown in Fig. 3. All cations and anions are in a slightly distorted octahedral environment. The final discrepancy factors and χ^2 are not very low because of the strongly disordered character of structure. The anomalous shape of the superlattice reflections (see, *e.g.*, the 2Θ range of 20–33°) indicates a significant fraction of stacking faults, typical of this class of compounds.[30,35–37] The ordered arrangement of cations shown in the left part of Fig. 1 is incompatible with the $C2/m$ symmetry. On the other hand, disordered Li^+/Fe^{3+}/Sb^{5+} arrangement would result in multiple Sb^{5+}–Sb^{5+}, Fe^{3+}–Fe^{3+} and additional Sb^{5+}–Fe^{3+} pairs sharing octahedral edges and violating the bond-valence principle. Therefore, we assume that each individual $(LiFeSbO_6)^{3-}$ layer is essentially ordered to avoid contacts of the polyvalent cations but the layer stacking is disordered resulting in the apparent $C2/m$ symmetry. The same assumption was used to explain apparent Na^+/Ir^{4+} mixing in Na_2IrO_3, *i.e.*, $Na_3(Na_2IrO_6)$, and other similar compounds.[35] Direct evidence of the almost ideal local order was received from the Mössbauer data (see the next section).

Mössbauer spectra

The ^{57}Fe Mössbauer spectrum (MS) of the Li_4FeSbO_6 sample, measured at T = 300 K, represents an asymmetric paramagnetic doublet with broadened components (Fig. 4a). The distribution function $p(\Delta)$ of the quadrupole splittings (Δ) has been restored to select the model for interpretation of the spectra.[41] The resulting function $p(\Delta)$ (Fig. 4b) has three peaks, indicating that the iron atoms occupy three nonequivalent positions with the average quadrupole splittings $\langle\Delta_1\rangle \approx 0.48$ mm s^{-1}, $\langle\Delta_2\rangle \approx 0.95$ mm s^{-1} and $\langle\Delta_3\rangle \approx 1.37$ mm s^{-1} respectively. Based on the results of the $p(\Delta)$ profile analysis, we can describe the experimental spectrum as a superposition of three quadrupole doublets Fe(1), Fe(2) and Fe(3) with the same values of isomer shifts ($\delta_1 = \delta_2 = \delta_3$) and linewidth ($\Gamma_1 = \Gamma_2 = \Gamma_3$), but significantly different quadrupole splittings (Δ_i) (Fig. 5a). The best-fit hyperfine parameters (δ, Δ_i, Γ) and relative intensities (I_i) of the partial spectra are listed in Table 2.

The isomer shifts of all resolved quadrupole doublets correspond to the high-spin Fe^{3+} ($3d^5$, S = 5/2) cations in the (FeO_6) sites coordinated octahedrally.[44] However, the noticeably different quadrupole splitting parameters Δ_i indicate that the Fe^{3+} cations in the Li_4FeSbO_6 structure are distributed over positions with different local symmetry of anionic polyhedra. Taking into account the proportion between the intensity of the partial subspectra $I_1/(I_2 + I_3) > 8$, we should assume that the Fe(1) doublet, with the smallest quadrupole splitting, arises from the Fe^{3+} cations occupying the most symmetrical regular position surrounded by 3 Li^+ and 3 Sb^{5+} cations. The second doublet Fe(2) can be attributed to the "antisite" positions of Fe^{3+} cations substituted for Li^{3+} or Sb^{5+} cations. It should be noted that each antisite Fe^{3+} substituting for a neighboring Li^+ or Sb^{5+} cation has two neighboring Fe^{3+} in

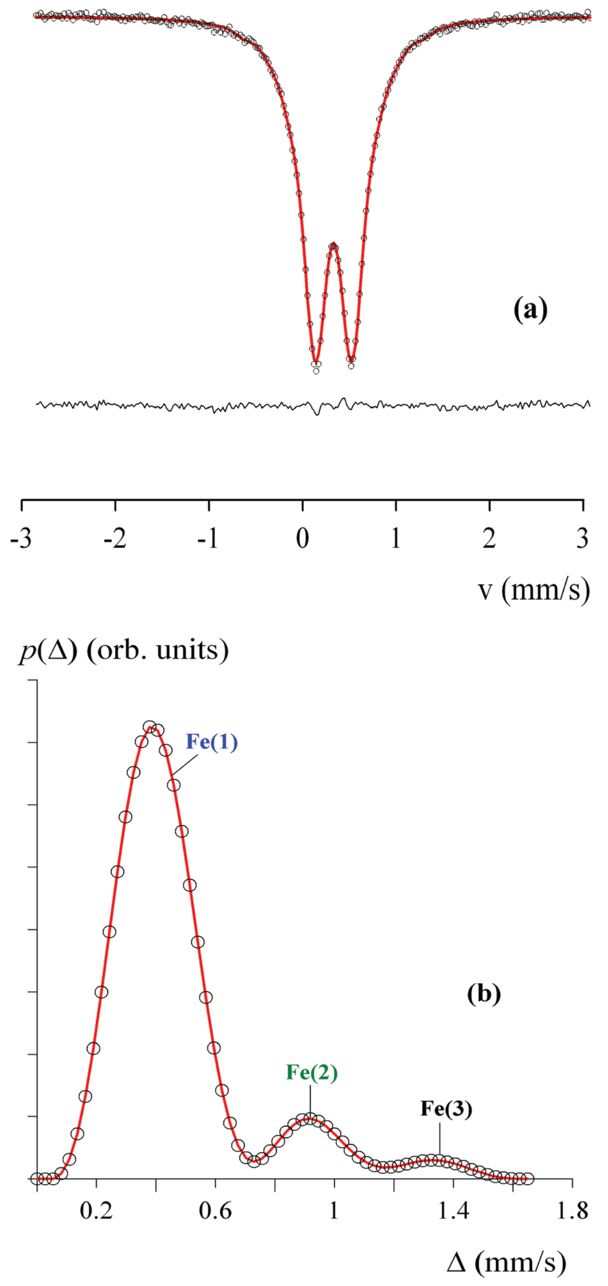

Fig. 4 The ^{57}Fe Mössbauer spectrum of the sample Li_4FeSbO_6 recorded at T = 300 K (a); distribution functions of the quadrupole splitting $p(\Delta)$ (b).

"regular" positions as shown in Fig. 6. These two ions should be influenced by the adjacent defect. The third quadrupole doublet Fe(3) with largest quadrupole splitting (Table 2) corresponds to Fe^{3+} cations stabilized in a very distorted oxygen surrounding. Thus, this partial spectrum can arise either from the Fe^{3+} cations with reduced oxygen coordination (near the oxygen vacancy), or from the iron cations located at the surface of the Li_4FeSbO_6 grains. Due to the small contribution of the Fe(3) subspectrum, it is difficult to accurately determine its hyperfine parameters.

To independently verify the correctness of the assignment of the partial spectra Fe(i) to the corresponding positions of iron cations in the crystal lattice of Li_4FeSbO_6, we calculated a lattice contribution to the electric field gradient (EFG) at Fe^{3+} cations in "regular" sites Fe^{3+} and "antisite" $Li^{+}(\leftarrow Fe^{3+})$ or $Sb^{5+}(\leftarrow Fe^{3+})$ positions. Moreover, the calculations of the EFG were carried out in a virtual position of the iron cation having one oxygen vacancy in its nearest anionic surrounding. Calculations of the EFG tensor have been realized within the ionic model in view of monopole contributions from each t-ion, occupying crystallographically non-equivalent positions. Crystallographic parameters used in the calculations have been taken from Table 1. Components (V_{ij}) of a tensor were calculated as follows:

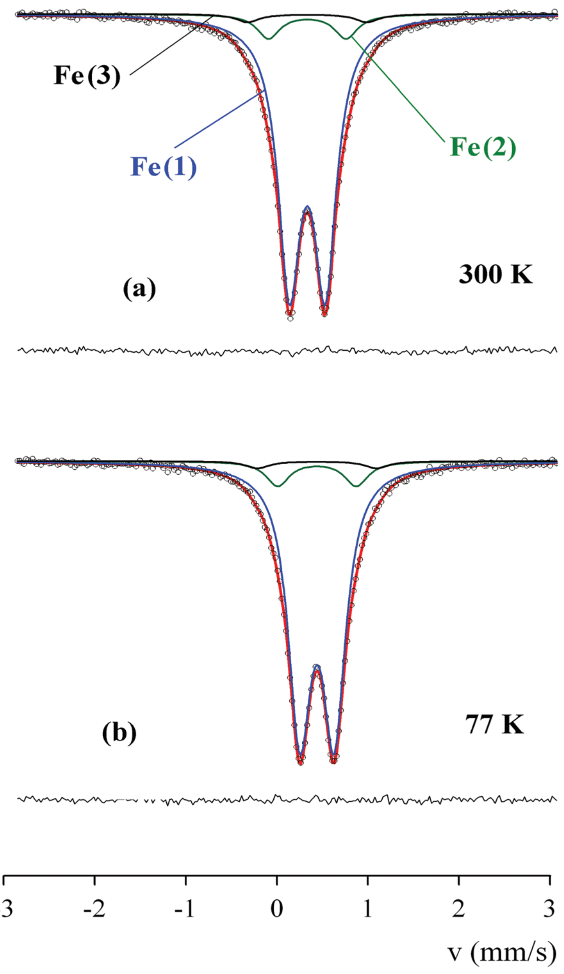

Fig. 5 Modelling reconstruction of ^{57}Fe Mössbauer spectra of the Li_4FeSbO_6 sample recorded at temperatures 300 K (a) and 77 K (b).

$$V_{ij} = (1-\gamma_\infty)\sum_t Z^t\left(\sum_{k(t)} \frac{3x_i^k x_j^k - \delta_{ij}(r^k)^2}{(r^k)^5}\right) \tag{1}$$

where Z^t is the charge of the t-ion, $k(t)$ is the summarized index on all positions of the t-ion, x_i^k and r^k are the Cartesian coordinates and radius-vector of the t-ion in position $k(t)$, δ_{ij} is the Kroneker symbol, and γ_∞ corresponds to Schterheimer's antishielding ($\gamma_\infty = -9.14$)[45] factor. The EFG tensors, calculated

Table 2 Hyperfine parameters of the ^{57}Fe Mössbauer subspectra for Li_4FeSbO_6

T (K)	Position	δ (mm s^{-1})	Δ (mm s^{-1})	Γ (mm s^{-1})	I (mm s^{-1})
300	Fe(1)	0.33 ± 0.01[a]	0.38 ± 0.01	0.31 ± 0.01[a]	89.1 ± 0.9
	Fe(2)	0.33[a]	0.86 ± 0.02	0.31[a]	8.5 ± 0.6
	Fe(3)	0.33[a]	1.30 ± 0.02	0.31[a]	2.4 ± 0.4
77	Fe(1)	0.44 ± 0.01[a]	0.4 ± 0.01	0.30 ± 0.01[a]	88.9 ± 0.7
	Fe(2)	0.44[a]	0.85 ± 0.02	0.30[a]	8.3 ± 0.4
	Fe(3)	0.44[a]	1.31 ± 0.02	0.30[a]	2.8 ± 0.4

[a] These parameters were taken equal to each other.

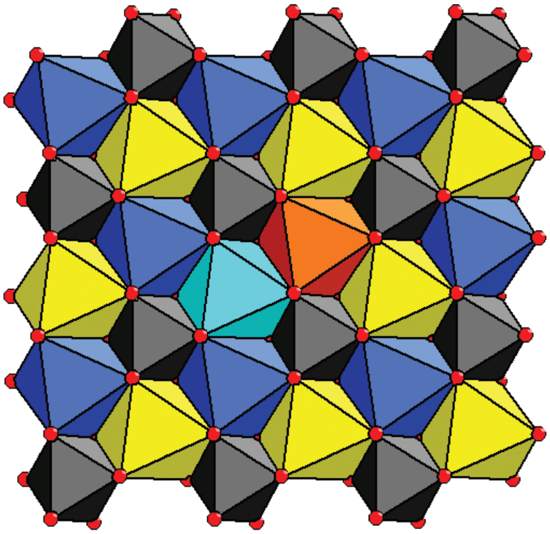

Fig. 6 A schematic of an antisite defect, Fe_{Li} + Li_{Fe}, resulting in two Fe–Fe contacts. Gray polyhedra, Sb; yellow and dark blue polyhedra, regular Fe and Li sites, respectively; orange and cyan polyhedra, antisite positions, Fe_{Li} and Li_{Fe}, respectively.

for each ^{57}Fe nucleus localized in the corresponding crystallographic positions of Fe^{3+} ions of the Li_4FeSbO_6 structure, have been used to estimate the quadrupole splitting values Δ for the subspectra Fe(1), Fe(2) and Fe(3):

$$\Delta = \frac{eV_{zz}Q}{2}\left(1 - \frac{\eta^2}{3}\right)^{1/2} \tag{2}$$

where eQ is the nucleus quadrupole moment (for ^{57}Fe eQ = 0.14 barn);[45] V_{zz} is the main component of the EFG tensor; $\eta \equiv (V_{xx} - V_{yy})/V_{zz}$ is the parameter of asymmetry.

The quadrupole splittings calculated by eqn (2), $\Delta_1^{(\text{theor})}$ = 0.58 mm s^{-1}, $\Delta_2^{(\text{theor})}$ = 0.98 (0.94) mm s^{-1} and $\Delta_3^{(\text{theor})}$ = 1.26 mm s^{-1}, correspond to the Fe^{3+} cations in the "regular" sites, $Fe^{3+} \rightarrow Li^{+}$ ($Fe^{3+} \rightarrow Sb^{5+}$) substitutions, and the Fe^{3+} sites located near the oxygen vacancy, respectively. At least two main factors are responsible for the discrepancy between the $\Delta_i^{(\text{theor})}$ and $\Delta_i^{(\text{exp})}$ (Table 2) magnitudes: (i) the uncertainty in choosing the effective charges Z^t (see eqn (1)) on the ions; (ii) the overlap of the filled 3p and 3d orbitals of the Fe^{3+} cations with the O^{2-} ligand orbitals also contributes to the discrepancy observed.[46] However, our calculations correctly predict the ratio of the Δ_i values (for example $\Delta_1^{(\text{theor})}/\Delta_2^{(\text{theor})} \approx 0.60$ is in good agreement with the experimental value $\Delta_1^{(\text{exp})}/\Delta_2^{(\text{exp})} \approx 0.44$, see Table 2). Thus, we can assure that the model used for the deconvolution and interpretation of the experimental spectrum is fully adequate and its subspectra Fe(i) are correctly assigned to definite positions of Fe^{3+} cations in the Li_4FeSbO_6 lattice.

The Mössbauer spectra measured in the temperature range 10 K $\leq T <$ 300 K, including the point $T \approx$ 100 K at which the ESR spectra undergo significant changes (see below sections on the ESR study), did not reveal any features (Fig. 5b). The line shape of the experimental spectra, as well as the hyperfine parameters of the Fe(i) subspectra remain practically unchanged (see Table 2). The isomer shift exhibits the usual increase with decreasing temperature due to the second-order Doppler shift (δ_{SOD}), which adds to isomer shift δ_{el} depending on the electron density at the ^{57}Fe nucleus.[44] Thus, according to the Mössbauer (MS) data, the iron cations remain in the paramagnetic state below $T \approx$ 100 K. Such a discrepancy between MS and ESR data (see below) may be due to the different values of the characteristic time scale (τ) of these methods ($\tau_{\text{MS}} \sim 10^{-8}$ s and ($\tau_{\text{ESR}} \sim 10^{-11}$ s).[47] We speculate that the frequency of the electronic spin fluctuations ω_{el} is significantly larger than the $\tau_{\text{MS}}{}^{-1}$ value resulting in "average" paramagnetic structure of the MS spectra. At the same time $\omega_{\text{el}} \approx \tau_{\text{ESR}}{}^{-1}$, thus when at $\omega_{\text{el}} \leq \tau_{\text{ESR}}{}^{-1}$ in the ESR spectrum line broadening may appear reflecting the appearance of the short-range magnetic interactions.

Electrochemical characterization

The electrochemical activity of Li_4FeSbO_6 was studied by means of cyclic voltammetry in the potential range between 2.9 V and 4.5 V. In Fig. 7, the first cycle is shown. The data imply a well defined redox couple at 4.3 V (ox.) and 3.9 V (red.). The sparsely pronounced hump above 4.4 V cannot be associated with a reversible oxidation process since a corresponding reduction peak is not observed. Generally, in order to maintain charge neutrality, the valences of the electrochemically active ions change upon lithium extraction. In the case of oxidation which is the first process occurring in the CV when increasing the potential from the starting potential 2.9 V, the only oxidisable species are the iron ions. In the subsequent reduction process appearing upon decreasing the potential from 4.5 V, most supposedly the same process is reversed. Therefore, the

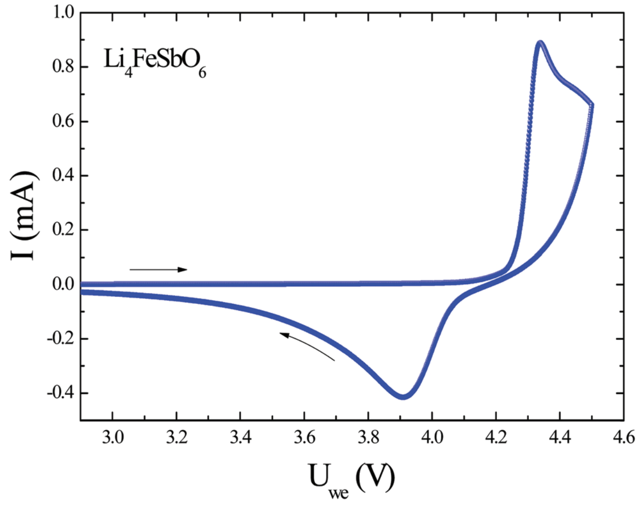

Fig. 7 Cyclic voltammogram (1st cycle) for Li_4FeSbO_6 performed with a scan rate of 0.1 mV s^{-1}.

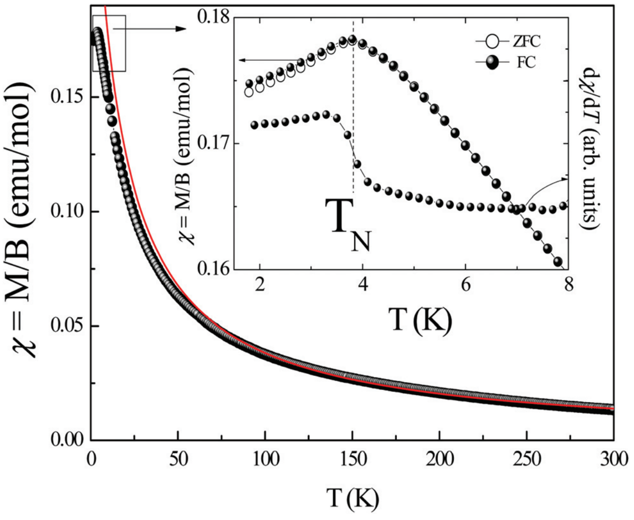

Fig. 8 Temperature dependence of the static magnetic susceptibility $\chi = M/B$ at B = 0.1 T for Li_4FeSbO_6. The solid red line represents a Curie–Weiss fit of the high-temperature data. The inset highlights the low temperature part of the magnetic susceptibility recorded in zero-field-cooled (ZFC) and field-cooled (FC) regimes and its derivation $d\chi/dT$.

possible active redox couple to be attributed to the observed reversible process is Fe^{3+}/Fe^{4+}.

In $LiFeO_2$ where the Fe^{3+}/Fe^{4+} redox couple is active[48] it appears at similar voltages as found here in Li_4FeSbO_6, whereas the potential regions of Fe^{2+}/Fe^{3+} are lower. For example, in $LiFePO_4$ it appears around 3.5 V.[49] Note that the observation of the Fe^{3+}/Fe^{4+} redox couple is confirmed by the analysis of the Mössbauer data presented above which implies Fe^{3+} ions in the pristine material. However, three nonequivalent (but somehow similar) positions for Fe as detected by the Mössbauer studies which might yield very tiny differences in the redox potentials cannot be resolved from our data.

Static magnetic properties

The static magnetic susceptibility $\chi = M/B$ of Li_4FeSbO_6 is presented in Fig. 8. The pronounced maximum at T_N = 3.6 K indicates the onset of long-ranged antiferromagnetic order as corroborated by the specific heat data presented below. The Néel temperature was deduced from the maximum of $\chi(T)$ and was found to be ~3.6 K (see the inset in Fig. 8). Suggesting Curie–Weiss-type behavior in the paramagnetic phase, we have analyzed the high temperature part of $\chi(T)$ according to the Curie–Weiss law with addition of a temperature-independent term χ_0:

$$\chi = \chi_0 + \frac{C}{T - \Theta} \tag{3}$$

where C is the Curie constant and Θ is the paramagnetic Curie–Weiss temperature. We have estimated χ_0 as high as ~−1 × 10^{-4} emu mol^{-1} in accordance with the summation of Pascal's constants[50] for the ions constituting Li_4FeSbO_6.

The Weiss temperature estimated from the Curie–Weiss fit of the $\chi(T)$ dependence in the range 200–300 K is found to be negative $\Theta \sim -17$ K and quite large in absolute value (comparing with $T_N \sim 3.6$ K). It is consistent with the dominance of antiferromagnetic coupling and the possible presence of a weak frustration in this compound. When lowering the temperature, $\chi(T)$ deviates from the Curie–Weiss-type behavior showing the increasing relevance of antiferromagnetic interactions upon approaching T_N from above. The effective magnetic moment μ_{eff} can be estimated from the Curie constant in accordance with

$$\mu_{\text{eff}}^2 = 3k_B C/\mu_B^2 N_A \tag{4}$$

where k_B is the Boltzmann constant, μ_B is the Bohr magneton and N_A is the Avogadro number. We have obtained μ_{eff} to be 5.93 μ_B/f.u., which is in excellent agreement with theoretical estimations assuming that the magnetism in Li_4FeSbO_6 is associated with Fe^{3+} (S = 5/2) ions:

$$\mu_{\text{theor}}^2 = g^2\mu_B^2 nS(S+1) \tag{5}$$

where g = 1.99 is the g-factor (experimentally determined in the present work from the ESR data – see below).

Careful study of the $M(T)$ dependence in the low temperature range under variation of the magnetic fields up to 7 T has shown that the character of the $M(T)$ dependence becomes more complicated with increasing magnetic field and two distinct anomalies can be identified at low temperatures (Fig. 9).

It was revealed that applying the magnetic field ~0.5 T leads to broadening of the maximum on the $M(T)$ dependence, and then this maximum splits into two peaks upon further increase of the magnetic field. With increasing external field, the two peaks separate increasingly. A slightly broader and weaker left peak (T_2) shifts toward the low-temperature side with increasing magnetic field and becomes almost undetectable in the fields above 4.5 T in the temperature range 1.8–6 K, whereas a sharper right peak (T_N) shifts toward the higher temperatures approximately up to 4.5 T, then changes the trend upon further increase of the applied magnetic fields.

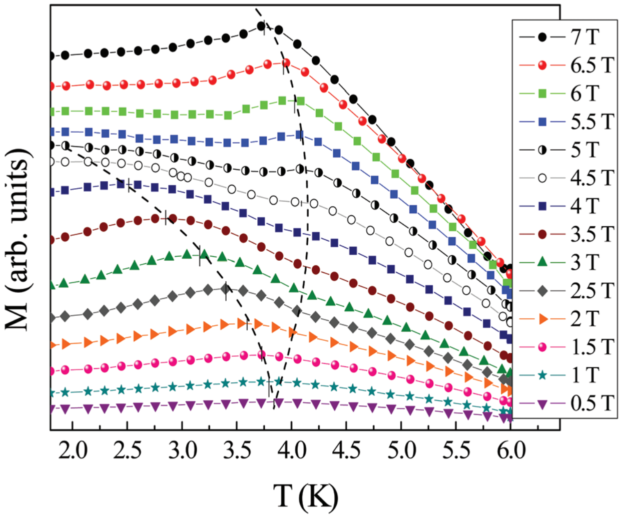

Fig. 9 $M(T)$ curves for Li_4FeSbO_6 at various external magnetic fields. The dashed lines show the position of the anomalies indicating their shift upon variation of the magnetic field.

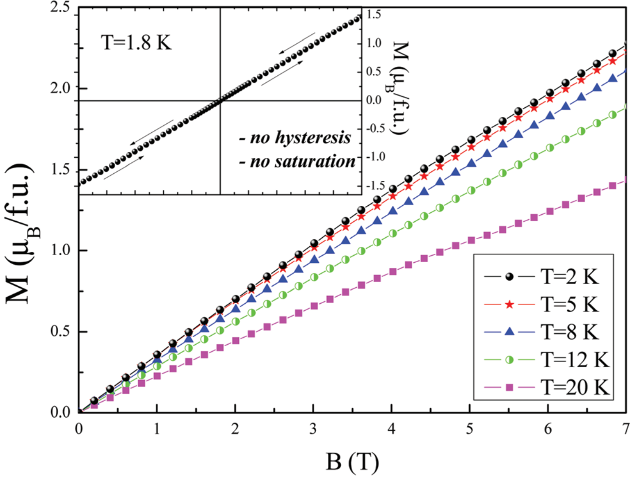

Fig. 10 Magnetization curves for Li_4FeSbO_6 at various temperatures. Inset: The full $M(B)$ isotherm at $T = 1.8$ K.

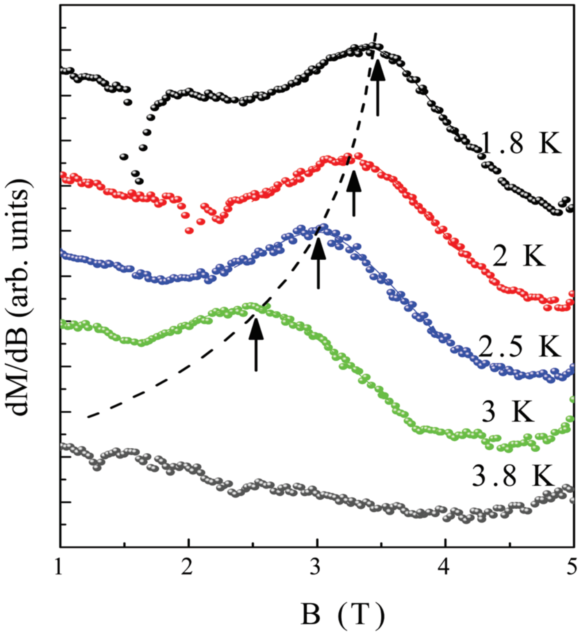

Fig. 11 The magnetization derivative dM/dB for Li_4FeSbO_6 at $T = 1.8$, 2, 2.5, 3 and 3.8 K. The dashed line and arrows indicate the position of spin-reorientation transition, observed at $T < T_N$.

The presence of two features is defined most clearly for the intermediate fields ~3–4 T. It is also worth mentioning that the effect is well reproducible using another sample.

Such behavior obviously indicates the complex nature of the magnetic ordering in the system investigated. Two critical temperatures, T_N and T_2, seem to correspond to two transitions at low temperatures. The latter, field-induced, may be associated with the spins reorientation under the magnetic field in a frustrated triangular lattice. Also note that the broader character of the anomaly at T_2 may be reflected in its possible low-dimensional (2D) correlation nature.

In addition to the tiny hysteresis which is already visible in the FC/ZFC $\chi(T)$ data in Fig. 8, the magnetization isotherms $M(B)$ do not display hysteresis or show saturation in magnetic fields up to 7 T (Fig. 10). Within this range of the applied magnetic fields, the magnetic moment is still far below the theoretically expected saturation magnetic moment for Fe^{3+} ($S = 5/2$):

$$M_s = gS\mu_B \approx 5\mu_B \qquad (6)$$

A more detailed inspection of the data reveals a rather broad but clear maximum in the derivative dM/dB which implies a slight left-bending in $M(B)$ at around 3 T (Fig. 11). Such features are indicative of a magnetic field induced spin-reorientation in Li_4FeSbO_6. Note that the maximum in dM/dB corresponds to the anomaly at T_2 in $M(T)$. Interestingly, the spin-anisotropy features are very broad. Similarly broad features have been observed in $La_5Ca_9Cu_{24}O_{41}$ in a region of the phase diagram where long-range antiferromagnetic order is replaced by short-range antiferromagnetic spin correlations.[51] In general, the larger the width of the spin-reorientation feature the smaller the spin-correlation length. Hence, one might speculate that the antiferromagnetic regions subjected to spin-reorientation in Li_4FeSbO_6 do not exhibit fully developed long-ranged spin order.

Such types of spin-reorientation transitions have been observed previously in related antimonates with cobalt ($Na_3Co_2SbO_6$)[31] and nickel ($Li_3Ni_2SbO_6$),[30] where the magnetic cations are ordered in the “honeycomb”-type lattice, which is a sort of triangular geometry. Similarly to these compounds the anisotropy peak position shifts towards lower fields upon increasing the temperature and eventually disappears above the Néel temperature. Note, however, that in contrast to Ni^{2+} and Co^{2+} the pure spin Fe^{3+} ion in an octahedral coordination as realized in Li_4FeSbO_6 is not supposed to exhibit spin

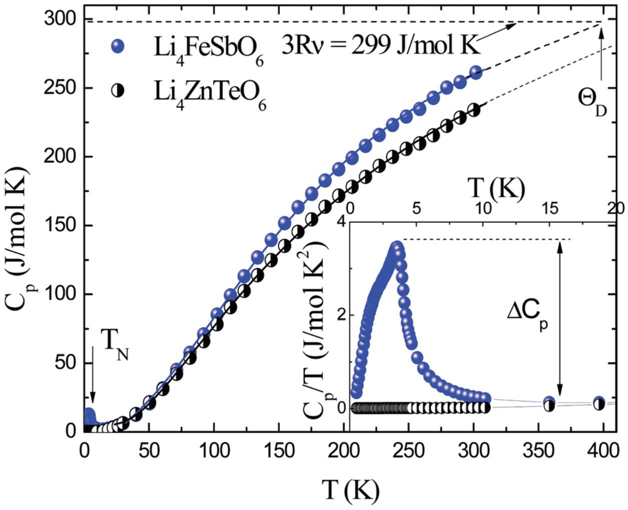

Fig. 12 Temperature dependence of the specific heat in Li_4FeSbO_6 (blue filled circles) and non-magnetic isostructural analogue Li_4ZnTeO_6 (black half-filled circles) in zero magnetic field. The inset highlights the onset of antiferromagnetic spin ordering at low temperatures and shows the specific heat jump ΔC_p.

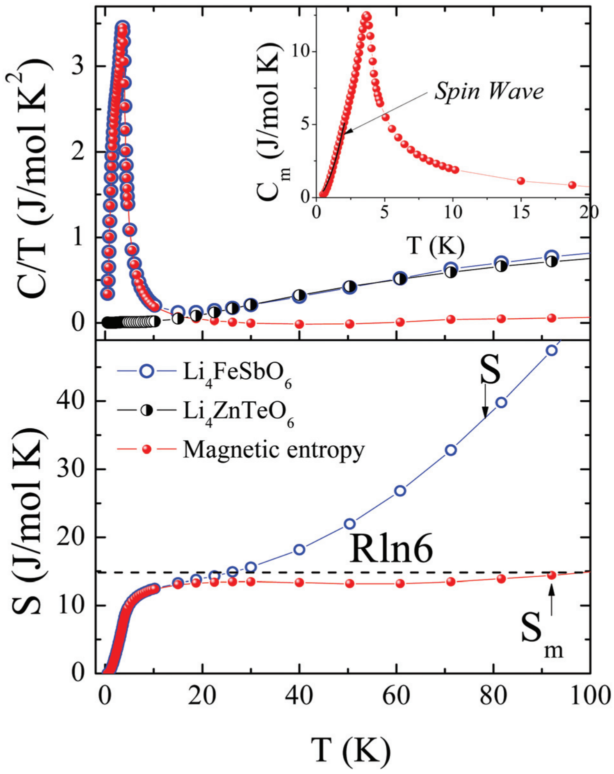

Fig. 13 Magnetic specific heat (red filled circles in the upper panel) and magnetic entropy (red filled circles in the lower panel) in comparison with the specific heat data for Li_4FeSbO_6 (blue open circles) and non-magnetic isostructural analogue Li_4ZnTeO_6 (black half-filled circles) at B = 0 T. In the inset: the low-temperature part of magnetic specific heat. The solid curve indicates the spin wave contribution estimated in accordance with eqn (8).

anisotropy. Detailed understanding of this issue will require further study preferably on the single crystals.

Temperature dependence of specific heat in applied magnetic fields

To clarify the complex nature of the features revealed from the magnetization study, comprehensive investigation of the specific heat was carried out in applied external magnetic fields up to 9 T. Specific heat data in zero magnetic field are in good agreement with the temperature dependence of magnetic susceptibility in weak magnetic fields, and demonstrate a distinct peak, related to an onset of the magnetic order at $T = T_N$ (Fig. 12). It should be noted though that the character of this peak is not typical of a sharp λ-shaped anomaly characteristic of second order phase transition (see the inset in Fig. 12). One can distinguish an additional weak anomaly at $T_m \sim 2.3$ K on the left-side shoulder of the major peak. At first glance, taking into account the magnetization data obtained, it seems natural to associate this anomaly with the spin reorientation below T_N. However, the positions of the T_m and T_2 peaks do not match at $B > 4$ T and shift in different ways with further increasing magnetic field as will be shown below in this section. Thus, the precise nature of the T_m anomaly remains to be elucidated at this point and will be additionally discussed below.

We observe a specific heat jump of $\Delta C_p \approx 13.5$ J mol^{-1} K^{-1}. This value is a bit less than the jump of ΔC_p, which is predicted from the mean-field theory for the antiferromagnetic spin ordering assuming iron to be in the Fe^{3+} ($S = 5/2$) state:[52]

$$\Delta C_p = 5R\frac{S(S+1)}{S^2+(S+1)^2} \approx 19.6 \text{ J mol}^{-1}\text{ K}^{-1} \tag{7}$$

where R is the gas constant $R = 8.31$ J mol^{-1} K^{-1}. Note that such a reduction of ΔC_p may indicate the presence of short-range magnetic correlations at higher temperature in Li_4FeSbO_6.

For quantitative estimations the specific heat data were measured also for the non-magnetic isostructural analogue Li_4ZnTeO_6. We assume that the specific heat of the isostructural compound Li_4ZnTeO_6 provides an estimate for the pure lattice contribution to specific heat. The correction to this contribution for Li_4FeSbO_6 has been made taking into account the difference between the molar masses for each type of atom in the compound (Zn–Fe and Te–Sb). The values for Debye temperature Θ_D have been determined as about ∼406 ± 1 K for the diamagnetic compound Li_4ZnTeO_6 and ∼399 ± 1 K for the Li_4FeSbO_6 respectively.

The magnetic contribution to the specific heat was determined by subtracting the lattice contribution using the data for the isostructural non-magnetic analogue Li_4ZnTeO_6 (Fig. 13). Note that the small value of the Néel temperature and the presence of two closely located anomalies at very low temperature essentially complicate any quantitative analysis of the specific heat behavior. Nevertheless we tried to make a trivial inspection of the low-temperature part of $C_p(T)$ according to the spin-wave (SW) theory. In terms of the simple SW approach the limiting low-temperature behavior of the magnetic specific heat below transition temperature (T_N) can be analyzed using the following relation:[53]

$$C_{SW} \propto T^{d/n} \tag{8}$$

where C_{SW} is the low-temperature specific heat due to spin wave excitation, d stands for the dimensionality of the magnetic lattice and n is defined as the exponent in the dispersion relation $\omega \sim k^n$. For phonons and antiferromagnetic magnons $n = 1$, for ferromagnetic magnons $n = 2$. We have fitted our data according to eqn (8) and obtained $d = 1.9$ and $n = 1.0$ values (see the inset in Fig. 13). This result implies that the spins in the present compound order into the 2D antiferromagnetic state at the lowest temperatures below T_N. It is consistent with the picture inferred from the layered crystal structure of Li_4FeSbO_6.

The entropy change has been calculated using the equation

$$\Delta S_m(T) = \int_0^T \frac{C_m(T)}{T} dT \tag{9}$$

The variation of entropy with temperature is also presented in Fig. 13. One can see that the magnetic entropy ΔS_m saturates at about 20 K reaching approximately 15 J mol^{-1} K^{-1}. This value is in good agreement with the magnetic entropy change for the $S = 5/2$ spin system, where $\Delta S_m(T)$ is equal to $R \ln(2S + 1)$. One should note that the magnetic entropy released below T_N removes only about 40% of the saturation value. This indicates the presence of appreciable frustration in Li_4FeSbO_6 and the short-range correlations far above T_N, which is usually the characteristic feature of materials with lower magnetic dimensionality.[54]

Remarkable observations were made for the specific heat in an external magnetic field. Fig. 14 collects the total specific heat data in Li_4FeSbO_6 at various magnetic fields. As mentioned above even at zero magnetic field one can distinguish an additional anomaly at T_m. At lower fields the anomaly at $T_N = 3.67$ K remains sharp and slightly shifts toward the higher temperatures up to ~4 K at 4 T similarly to the magnetization data (Fig. 9). Upon further increase of the magnetic field it changes the trend and shifts to the low temperature side reduced down to a minimum value ~3.1 K at 9 T. At the same time, the flatter anomaly on the $C(T)$ curve at $T_m < T_N$ locates quite closely to the T_2 peak position in magnetic fields below ~4 T, but at higher fields its position seems to vary more weakly under variation of the magnetic field, so the presence of two features manifests most clearly in the intermediate field range (3–4 T).

Such an anomaly is possibly reminiscent of the anomalies observed for other frustrated systems with triangular geometry of the magnetic sublattice, for example in $PbMn_5(SO_4)_6$ and $SrMn_5(SO_4)_6$ [55] and in $CsFeBr_3$.[56] The authors of ref. 56 associated their findings with the coexistence of spin frustration and quantum fluctuations in the triangular magnetic structure.

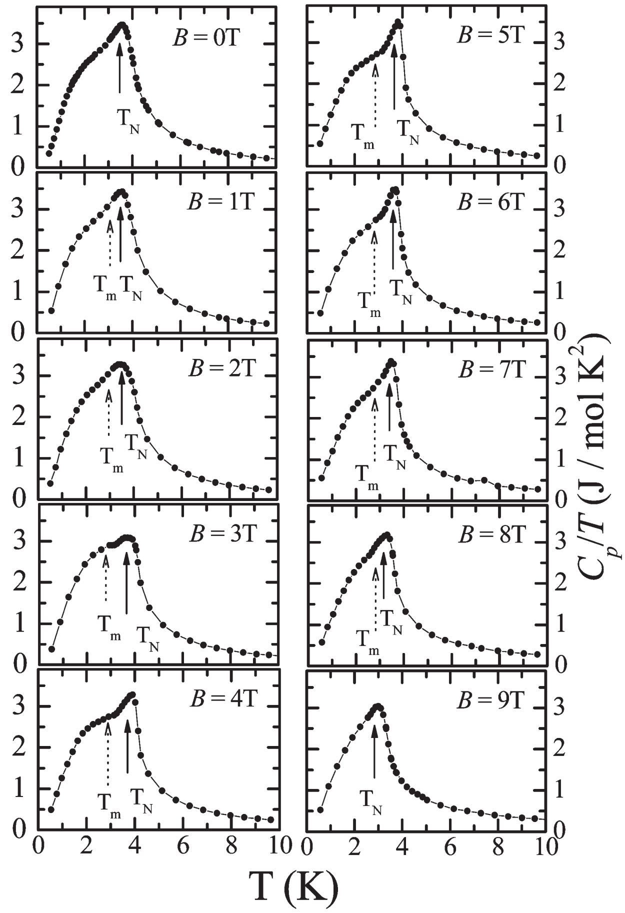

Fig. 14 Temperature dependence of the specific heat in Li_4FeSbO_6 at various magnetic fields. The arrows denote the transition temperatures T_N and T_m.

Dynamic magnetic properties

To further elucidate complex thermodynamic properties of the system under study we have performed the electron spin resonance study. Evolution of the ESR spectra of powder sample Li_4FeSbO_6 with temperature is presented in Fig. 15 at two different frequencies. The shape of the ESR line is changed visibly when the temperature decreases: the distortion and broadening of the ESR spectrum occur upon approaching the magnetic ordering temperature from above. An accurate analysis of the lineshape requires including two circular components of the exciting linearly polarized microwave field into the fit formula[57] since the line observed is relatively broad (only one order less than the resonance field in the present compound):

$$\frac{dP}{dB} \propto \frac{d}{dB}\left[\frac{\Delta B}{\Delta B^2 + (B - B_r)^2} + \frac{\Delta B}{\Delta B^2 + (B + B_r)^2}\right] \tag{10}$$

This is a symmetric Lorenzian line, where P is the power absorbed in the ESR experiment, B – magnetic field, B_r – resonance field, ΔB – the linewidth. Results of ESR lineshape fitting are shown by solid lines in Fig. 15. Apparently, the fitted curves are in good agreement with the experimental data.

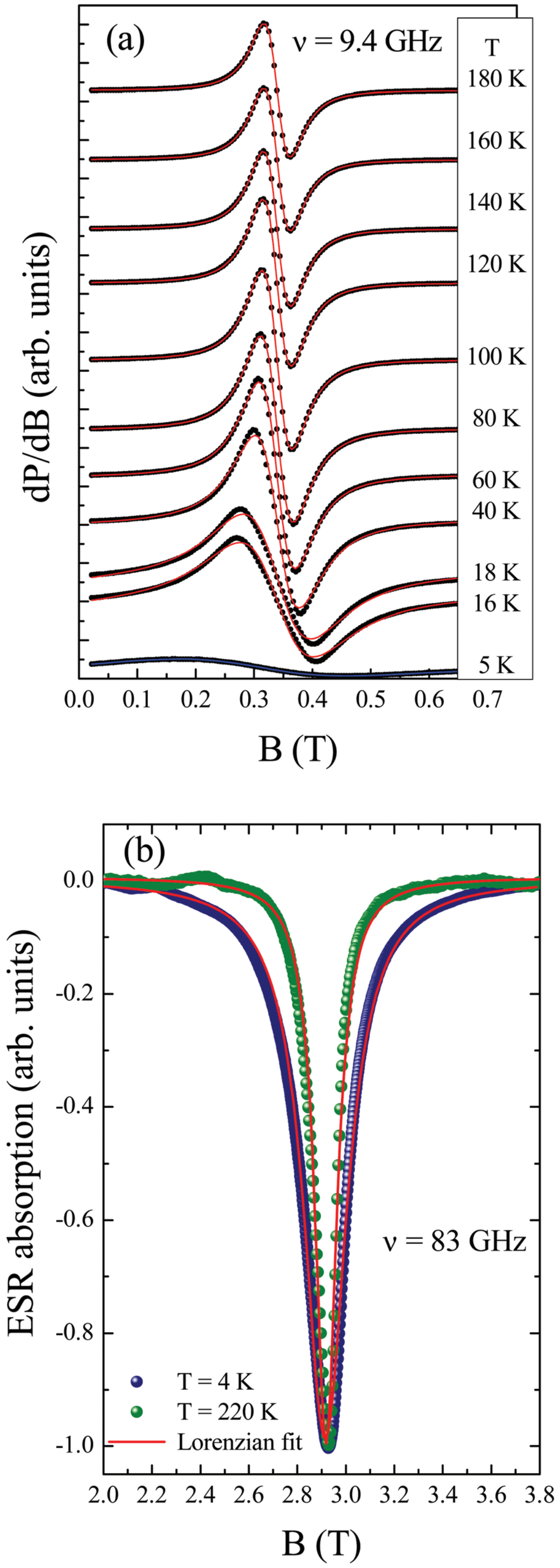

Fig. 15 Temperature evolution of the first derivative absorption line (a) and full ESR absorption (b) for Li_4FeSbO_6 antimonate at two different frequencies: points – experimental data, lines – fitting in accordance with the Lorenzian profile (eqn (10)).

At high temperatures (T > 100 K) the ESR spectra are satisfactorily described by a single Lorenzian, which is ascribable to Fe^{3+} ions in octahedral coordination. The effect of the nearest-neighbor oxygen ligands on the ESR properties of the Fe^{3+} ions can be represented by a spin Hamiltonian of the general form

$$\mathbf{H} = g\mu_B \vec{H} \cdot \vec{S} + b_2^0\left[S_z^2 - \frac{1}{3}S(S+1)\right] + \\ + \frac{1}{6}b_2^1(S_xS_z + S_zS_x) + \frac{1}{3}b_2^2\left(S_x^2 - S_y^2\right) \tag{11}$$

where g is the g-factor, S is the spin and the parameters b_2^n are the crystal-field splitting constants related to the symmetry of the ligand field. The parameters b_2^n can be expressed as a linear superposition of axially symmetric contributions from the individual ligand ions. It is well known that for the Fe ($3d^5$) free ion the orbital angular momentum is zero and the ground state is sixfold degenerate, S = 5/2.[58,59] In octahedral oxygen complexes with the point symmetry O_h, the parameters b_2^n are close to zero ($b_2^0 = b_2^1 = b_2^2 = 0$) hence an ESR line at g = 2 is expected.[60] Although the local symmetry of the (Fe,Li) site in the Li_4FeSbO_6 is different from O_h, distortions of the octahedra are not very big (bond lengths being in the range 2.14–2.17 Å). Indeed, at high temperatures we observed a single absorption line, which is characterized by the isotropic g-factor value $g = 1.99 \pm 0.01$.

Upon cooling the samples below ~100 K one can see a gradual deviation of the ESR signal shape from the Lorentzian form, which probably indicates the suppression of the exchange narrowing effect due to the slowing down of the spin–spin correlations by approaching the short-range ordering regime. Temperature dependencies of the effective g-factor and the linewidth derived from the fitting according to eqn (10) together with the frequency–field $f(B)$ diagram at 100 K are collected in Fig. 16. The data obtained at different frequencies are in reasonable agreement with each other. The $f(B)$ dependence at 100 K demonstrates a linear gapless character typical of the paramagnetic state with a g-value of about 2.0. The effective g-factor remains practically constant down to low temperatures and visible shift of the resonant field accompanied by the signal fading occurs only at helium temperature. This could be indicative of the opening of an energy gap for resonance excitations due to the establishment of AFM order. At the same time, we observe an essential broadening of the resonance mode over the whole temperature range investigated. Apparently, such behavior indicates the presence of strong short-range correlations essentially higher than ordering temperature, those are characteristic of the low-dimension systems.

The integral ESR intensity (not shown), which is proportional to the number of magnetic spins, was estimated by the double integration of the first derivative ESR spectrum for each temperature. It was found that the integral ESR intensity χ_{esr} in the paramagnetic phase varies with temperature in accordance with the Curie–Weiss law and agrees quite well with behavior of the magnetic susceptibility χ.

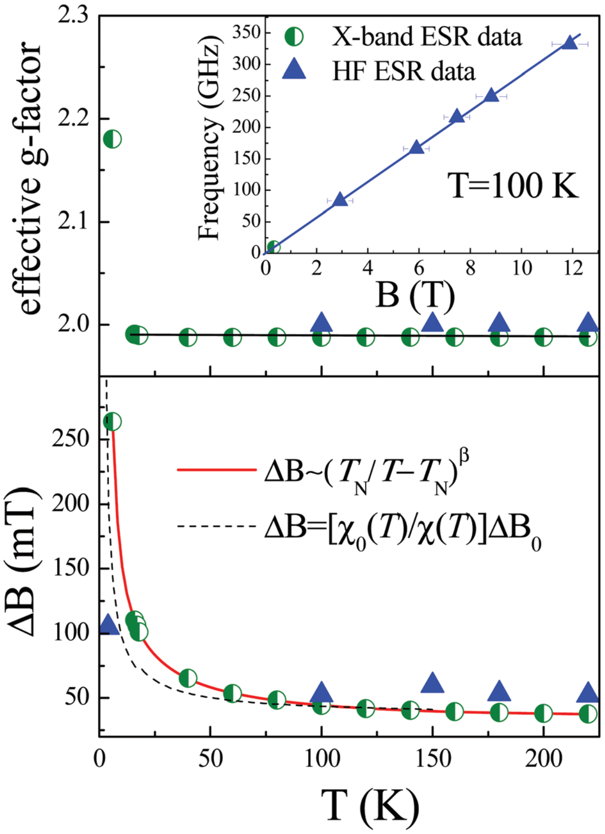

Fig. 16 Temperature dependencies of the effective g-factor and the ESR linewidth ΔB for Li_4FeSbO_6 derived from the fitting in accordance with eqn (10). In the inset: frequency–field diagram at 100 K. Solid and dashed curves on the lower panel are the approximations of $\Delta B(T)$ dependence according to models of the critical fluctuations [eqn (12) and (13)].

Critical behavior of ESR linewidth

The ESR linewidth (lower panel in Fig. 16) was revealed to exhibit a rapid increase as temperature decreases, most pronounced at temperatures below 50 K. Such an increase of the ΔB is usually observed in the antiferromagnets due to the slowing down of spin fluctuations as the critical temperature is approached from above.[61–63] The latter causes the divergence of the spin correlation length, which in turn affects the spin–spin relaxation time of exchange narrowed ESR lines resulting in the critical broadening of the ESR line in the vicinity of T_N. In this case, the temperature variation of ΔB can be described by

$$\Delta B(T) = \Delta B^* + A\left[\frac{T_N^{ESR}}{T - T_N^{ESR}}\right]^{\beta} \tag{12}$$

where the first term ΔB^* describes the high-temperature exchange narrowed linewidth, which is temperature independent, while the second reflects the critical behavior with T_N^{ESR} being the temperature of the order–disorder transition and β the critical exponent. In the frame of the Kawasaki approach[61] the critical exponent can be expressed as $\beta = -[1/2(7 + \eta)\nu - 2(1 - \alpha)]$ where ν describes the divergence of correlation length, η is a critical exponent for the divergence of static correlations and α reflects divergence of the specific heat, respectively. The best fit of the X-band ESR experimental data according to eqn (12) resulted in the values $\Delta B^* = 10$ mT, $T_N^{ESR} = 3.56$ K, $\beta = 0.58$. Apparently, the value of T_N^{ESR} is remarkably close to the Néel temperature $T_N = 3.6$ K, where the anomaly in the magnetic susceptibility and heat capacity has been observed. The value $\beta = 0.58$ is well comparable both with the values of 0.55 and 0.33 reported for other antiferromagnetic iron oxides[64,65] and with the value of 0.9 estimated for structurally related antimonate $Li_3Ni_2SbO_6$.[30]

A surprising result is the validation of the model [eqn (12)] in an extended T-range far above T_N. Continuous broadening of the ESR linewidth in an extended T-range ($3T_N \leq T \leq 10T_N$) has been previously observed for other systems, mainly for the antiferromagnetic insulators,[66] and has been mainly related to the temperature variation of the static susceptibility. In the paramagnetic regime far above the critical regions associated with the magnetic transition, where any critical contribution to $\Delta B(T)$ as well as spin–lattice relaxation (which is expected to be weak for S-state ions line Fe^{3+}) can be neglected, the temperature variation of the ESR linewidth can be described by the expression[66]

$$\Delta B(T) = \Delta B_0\left[\frac{\chi_0(T)}{\chi(T)}\right] \tag{13}$$

where $\chi_0 = C/T$ is the free single-ion susceptibility with C the Curie constant of the uncoupled paramagnetic system, while $\chi(T)$ is the static susceptibility of the coupled system and ΔB_0 describes the temperature-independent high-temperature limit of the linewidth associated with the contribution of anisotropic spin–spin interactions. To this aim, we have calculated the T variation of the ΔB using the measured dc susceptibility $\chi(T)$, the Curie constant, estimated as $C = N_A g^2 \mu_B{}^2 S(S + 1)/3k_B = 4.4$ emu K mol^{-1} per formula unit of Li_4FeSbO_6 with $S = 5/2$ and $g = 1.99$ for Fe^{3+} ions, and the constant value $\Delta B_0 = 38.6$ mT estimated in the high temperature limit (Fig. 16). Comparison with the experimental linewidth data shows that the static susceptibility may roughly account for the temperature evolution of the ΔB (black dashed curves in Fig. 16). However, appreciable deviation occurs as temperature decreases as compared both with experimental points and with the product of fitting in accordance with eqn (12), especially at low temperatures.

Bearing in mind that the considered Li_4FeSbO_6 compound has layered structure with triangular arrangement of the magnetic atoms, one can expect a possible effect of the dimensionality and the frustration not only on the static magnetic properties but also on dynamic ones. So, it seems worth analyzing the critical behavior also in the context of the Kosterlitz–Thouless scenario – one of the most important theoretical approaches developed for the layered systems. For the two-dimensional XY model, Kosterlitz and Thouless and independently Berezinskii (BKT model) predicted a topological phase transition caused by the unbinding of vortex–antivortex pairs at a certain transition temperature $T_{KT} < T_N$.[24–27] Experimentally the presence of this transition has been confirmed for several quasi-2D layered compounds with weak interplane interactions, *e.g.*, in the honeycomb lattices and $BaNi_2P_2O_8$,[67,68] $BaNi_2V_2O_8$ [69] and in $MnPS_3$.[70] *Via* Monte-Carlo simulations Kawamura and Miyashita (KM)[71] have shown that the topological defects in the case of 2D TLAFM have a different type – so-called Z_2-vortices. In contrast to the vortices considered in the XY BKT model where the topological quantum number, which indicates the number of circulations of spins within the vortex, can take any integer value, Z_2-vortices are characterized by a two-valued topological quantum number, only. In a 2D Heisenberg TLAFM, frustration is partially released by forming a local 120° spin structure. These short-range spin correlations give rise to an additional degree of freedom called the vector chirality, *i.e.*, left- or right-handed circulation, which leads to the formation of the Z_2-vortices. Recently, the temperature dependence of the correlation length between the Z_2 vortices has been found to be similar to the BKT case.[72,73] The proofs of Z_2-vortices have been obtained experimentally for 2D frustrated TLAFM in two recent works by Hemmida *et al.*[22,23] Being proportional to the third power of the correlation length[1] the ESR linewidth will be expressed as

$$\Delta B = \Delta B_\infty \exp\left(\frac{3b}{\tau^\nu}\right) \tag{14}$$

where ΔB_∞ is the asymptotic high-temperature value of the linewidth, b is an arbitrary parameter, ν = 0.5 in the frame of the classical BKT approach, while it takes slightly reduced values ν = 0.42[71] and ν = 0.37[74] for the triangular lattice, τ denotes normalized temperature:

$$\tau = \frac{T}{T_{KM}} - 1$$

with T_{KM} being the topological phase transition temperature above which the Z_2-vortices dissociate.

We fitted the linewidth data by eqn (14) setting ν = 0.42 and ν = 0.37, respectively, and taking ΔB_∞, T_{KM} and b as variable fit parameters (Fig. 17). Table 3 summarizes corresponding results. As one can see, the linewidth data are very well described by both exponents in the whole temperature range without adding any residual linewidth contribution. Looking closer at the results of fitting one can see that the R^2 value just slightly prefers the lower exponent ν = 0.37. In accordance with expectations, the estimations for the vortex-transition temperature T_{KM} yield values below T_N. Also note that the determined parameters b are in good agreement with the value b = π/2 theoretically predicted for the BKT critical regime and well comparable with b = 1.86, 1.93 values given for triangular antiferromagnets $CuCrO_2$ and $AgCrO_2$ respectively,[23] as well as with $b \approx 1$ reported for the quasi 2D honeycomb antiferromagnet $BaNi_2P_2O_8$.[69]

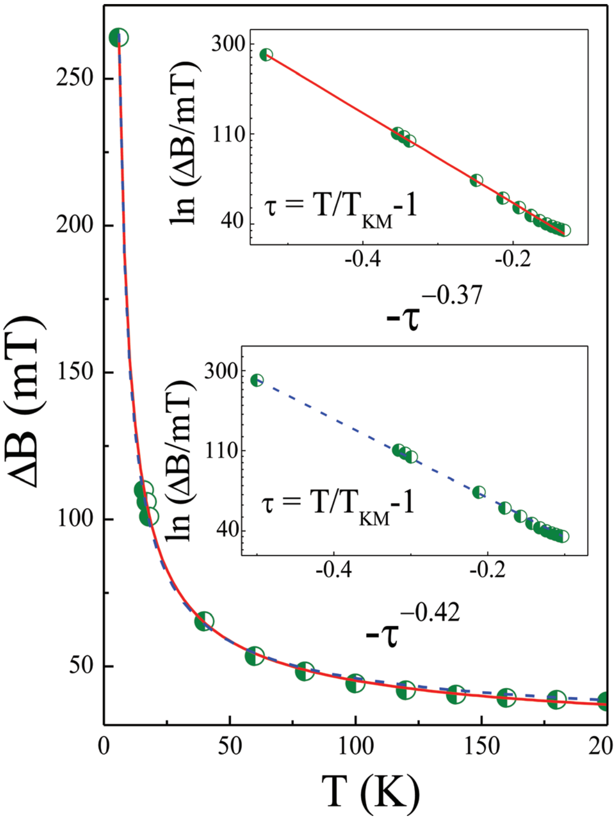

Fig. 17 Temperature dependencies of the ESR linewidth of ESR spectra of Li_4FeSbO_6. Solid and dashed curves are the fits of $\Delta B(T)$ dependence according to the KM model [eqn (14)] (described in the text). Insets: Logarithmic plots of $\ln(\Delta B)$ *vs.* $-\tau^{-\nu}$ evidence the validation of BKT-type critical behaviour (in the frame of KM theory) over the whole temperature range.

Table 3 Parameters determined from the fit of $\Delta B(T)$ according to the KM model [eqn (12)]

ν	ΔB_∞ (mT)	T_{KM} (K)	b	R^2
0.37	18.7	1.0	1.7	0.9999
0.42	22.8	1.1	1.6	0.9992

Thus, the analysis performed makes us anticipate the presence of Z_2-vortices down to BKT-type topological transition $T_{KM} < T_N$ in the Li_4FeSbO_6 compound. To support this idea one can look for a signature of BKT critical behavior from the thermodynamic properties described above. Quite often though such features are either too weak to be extracted or too close to the critical temperature to be experimentally accessible.[75] The interlayer coupling, even if orders of magnitude smaller than the intralayer one, drives the system towards a 3D transition, which is actually triggered by the divergence of 2D intralayer spin correlations. Therefore purely 2D critical behavior of diverging quantities is most often masked by the onset of 3D long-range order. Nevertheless, assuming the presence of the topological excitation in the form of vortices and antivortices in our system, one should expect that they will attract each other upon lowering the temperature until Z_2-vortices–antivortices pairs begin to form and a maximum in the specific heat will correspondingly occur. According to the

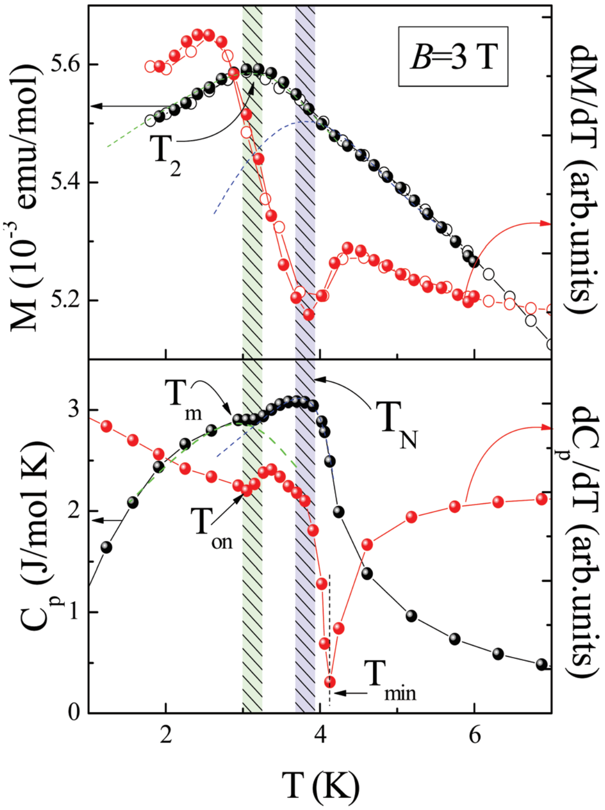

Fig. 18 Representative example of the determination of the anomalies from the temperature dependencies of magnetization and specific heat recorded in applied magnetic field $B = 3$ T. Vertical bars indicate the uncertainty in determination. Filled and open circles on the upper part correspond to the data measured for two different samples of Li_4FeSbO_6.

theoretical predictions such a maximum should be higher than the critical temperature T_{KM}, at which all Z_2-vortices and antivortices are paired and the topological transition occurs.[75,76] Indeed a closer inspection of our specific heat data shows that we have observed a flatter anomaly at T_m ($T_{KM} < T_m < T_N$), which, in fact, may also indicate the formation of Z_2-vortices down to BKT-type topological transition in quasi 2D TLAFM Li_4FeSbO_6.

Magnetic phase diagram

Summarizing the data of thermodynamic and resonance studies performed in the present work, the magnetic phase diagram for a new layered antimonate Li_4FeSbO_6 can be constructed. Fig. 18 represents an example of the analysis performed for the temperature dependencies of the magnetization and the specific heat. One can see that several different anomalies can be inferred. All anomalies obtained from this analysis together with the data from Fig. 11 are shown in Fig. 19. In zero magnetic field the paramagnetic phase is realized at temperatures higher than 3.6 K, while applying the magnetic field shifts this phase boundary initially toward the higher temperatures and then to the opposite side. Obviously, such character of the AFM-PM boundary moving directly indicates the low-dimensional nature of the correlations and frustration in Li_4FeSbO_6, when the external magnetic field raises the transition temperature due to suppression of the frustration. It is also evident from the B–T diagram that the ground state of Li_4FeSbO_6 is found to be antiferromagnetic but an intermediate magnetic phase (II) was induced by applying a magnetic field. Thus, there are at least two phases (I and II) related with probably two different spin orientations. It can be associated with the change of the mutual orientation of neighboring spins in the triangular lattice. Short-range triangular antiferromagnetic order maintained by the strong exchange interaction exists up to much higher fields, of the order of B_{sat} at $T = 0$ K. Indeed, the ordering temperature of Li_4FeSbO_6 is smaller than the absolute value of Curie–Weiss temperature $\Theta \approx -17$ K ($f = \Theta/T_N \sim 5$). Thus, the strong exchange correlations should survive in a broad temperature interval, characteristic for the wide critical range of low-dimensional systems that was confirmed from our ESR data. On the other hand the interplane exchange may also cause additional field-induced phase transitions, where the mutual orientation of spins in the neighboring planes changes. To elucidate further the complex phase diagram of the new compound Li_4FeSbO_6 a detailed study of single crystals is strongly desirable.

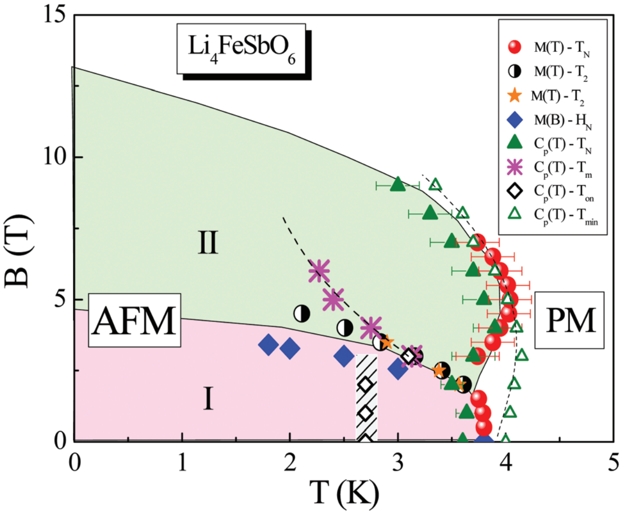

Fig. 19 The magnetic phase diagram for a new layered antimonate Li_4FeSbO_6.

Conclusions

In conclusion, we have successfully prepared and investigated a new layered antimonate Li_4FeSbO_6. The crystal structure was found to represent an ordered superlattice derived from the α-$NaFeO_2$ structure type with overall monoclinic ($C2/m$) symmetry. The magneto-active $(LiFeSbO_6)^{3-}$ layers alternate with nonmagnetic lithium layers in the structure. Each individual $(LiFeSbO_6)^{3-}$ layer is essentially ordered resulting in a triangular cell for the magnetic Fe^{3+} ions. Direct evidence of the almost ideal local order was received from the Mössbauer data. The isomer shifts correspond to the high-spin Fe^{3+} ($S = 5/2$) cations in the FeO_6 octahedra.

The static magnetic susceptibility data and specific heat ones show the onset of antiferromagnetic order at $T_N \approx 3.6$ K. Most of the entropy removal occurs at temperatures higher than T_N, indicating the presence of appreciable frustration and short-range correlations in the compound. The high-temperature magnetic susceptibility data exhibit Curie–Weiss behavior with a Weiss temperature taking a negative value $\Theta \sim -17$ K that indicates a predominance of the antiferromagnetic coupling and the frustration possibly triggered by a triangular geometry of the magnetic subsystem and essentially competing interplane and intraplane interactions. The effective magnetic moment is estimated to be 5.93 μ_B/f.u. and agrees with the estimations assuming high-spin configuration of Fe^{3+} ($S = 5/2$). At the same time, an additional field-induced transition has been revealed from temperature and field dependencies of the magnetization at temperature $T_2 < T_N$. The anomalies at T_N and T_2 separate increasingly on increasing the external field indicating field-sensitive moving of magnetic phase boundaries.

In agreement with the analysis of the magnetic data, cyclic voltammetry shows an Fe^{3+}/Fe^{4+} redox couple at 4.3 V (ox.) and 3.9 V (red.). The data imply that Li can be reversibly extracted.

ESR spectra in the paramagnetic phase show a single Lorenzian shape line attributed to Fe^{3+} ions in octahedral coordination characterized by the isotropic temperature independent effective g-factor $g = 1.99 \pm 0.01$. However, the distortion and broadening of the ESR absorption line were found to take place below ~100 K. The temperature dependence of the ESR intensity, linewidth and shift of the resonant field imply an extended region of short-range order correlations in the compound studied.

Anomalous broadening of the ESR linewidth upon decreasing the temperature was revealed over the whole temperature range investigated. Corresponding divergence of the temperature-dependent correlation length on approaching T_N from above was described in terms of both the critical behavior close to long-range magnetic order and assuming the Berezinskii–Kosterlitz–Thouless (BKT)-type transition in 2D TLAFM due to formation of topological defects in the form of Z_2-vortices. A signature of this type of transition is supposed to be traced also from the heat capacity data, which manifested the appearance of an additional anomaly of unknown nature below the T_N.

Thus, the results of both structural and magnetic studies performed here were well consistent with each other and allowed us to suggest a unique magnetic phase diagram in agreement with the frustrated and possibly easy-plane non-collinear antiferromagnetic nature of magnetic coupling for this new compound. The rich variety of the anomalies in magnetic and resonance properties makes Li_4FeSbO_6 an interesting system to investigate the multiple phase transitions and competing exchange interactions due to the critical role of the layered structure accompanied by the frustration effects in triangular antiferromagnets.

Acknowledgements

The authors would like to thank Dr V. Kataev, IFW, Dresden, Germany, for fruitful discussions of the ESR results. V.B.N. and M.A.E. appreciate support from the Russian Foundation for Basic Research (grant 11-03-01101) and the International Centre for Diffraction Data (grant-in-aid 00-15). J.Y.L. and C.N.K. acknowledge support from MOE-ATU and National Science Council of Taiwan under Grant No. NSC98-2112-009-005-MY3. R.K. and C.J. acknowledge support from the Bundesministerium für Bildung und Forschung *via* the LIB2015 alliance (Grant 03SF0397).

References

1 H. Benner and J. B. Boucher, in *Magnetic Properties of Layered Transition Metal Compounds*, ed. L. J. de Jongh, Kluwer Academic Publisher, Dordrecht, 1990.
2 K. Hirota, Y. Nakazawa and M. Ishikawa, *J. Phys.: Condens. Matter*, 1991, **3**, 4721.
3 S. J. Clarke, A. J. Fowdes, A. Harrison, R. M. Ibberson and M. J. Rosseinsky, *Chem. Mater.*, 1998, **10**, 372.
4 A. P. Ramirez, B. Hessen and M. Winklemann, *Phys. Rev. Lett.*, 2000, **84**, 2957.
5 T. Okuda, T. Kishimoto, K. Uto, T. Hokazono, Y. Onose, Y. Tokura, R. Kajimoto and M. Matsuda, *J. Phys. Soc. Jpn.*, 2009, **78**, 013604.
6 S. Nakatsuji, Y. Nambu, H. Tonomura, O. Sakai, S. Jonas, C. Broholm, H. Tsunetsugu, Y. Qiu and Y. Maeno, *Science*, 2005, **309**, 1697.
7 I. Terasaki, Y. Sasago and K. Uchinokura, *Phys. Rev. B: Condens. Matter*, 1997, **56**, R12685.
8 Y. Y. Wang, N. S. Rogado, R. J. Cava and N. P. Ong, *Nature*, 2003, **423**, 425.
9 K. Takada, H. Sakurai, E. Takayama-Muromachi, F. Izumi, R. A. Dilanian and T. Sasaki, *Nature*, 2003, **422**, 53.
10 S. Seki, Y. Onose and Y. Tokura, *Phys. Rev. Lett.*, 2008, **101**, 067204.
11 K. Kimura, H. Nakamura, S. Kimura, M. Hagiwara and T. Kimura, *Phys. Rev. Lett.*, 2009, **103**, 107201.
12 M. Kenzelmann, G. Lawes, A. B. Harris, G. Gasparovic, C. Broholm, A. P. Ramirez, G. A. Jorge, M. Jaime, S. Park, Q. Huang, A. Ya. Shapiro and L. A. Demianets, *Phys. Rev. Lett.*, 2007, **98**, 267205.
13 A. I. Smirnov, H. Yashiro, S. Kimura, M. Hagiwara, Y. Narumi, K. Kindo, A. Kikkawa, K. Katsumata, A. Ya. Shapiro and L. N. Demianets, *Phys. Rev. B: Condens. Matter Mater. Phys.*, 2007, **75**, 134412.
14 L. E. Svistov, A. I. Smirnov, L. A. Prozorova, O. A. Petrenko, L. N. Demianets and A. Ya. Shapiro, *Phys. Rev. B: Condens. Matter*, 2003, **67**, 094434.
15 A. I. Smirnov, L. E. Svistov, L. A. Prozorova, A. Zheludev, M. D. Lumsden, E. Ressouche, O. A. Petrenko, K. Nishikawa, S. Kimura, M. Hagiwara, K. Kindo, A. Ya. Shapiro and L. N. Demianets, *cond-mat*/0807.2804.

16 S. Mitsuda, M. Mase, K. Prokes, H. Kitazawa and H. Aruga Katori, *J. Phys. Soc. Jpn.*, 2000, **69**, 3513.

17 O. A. Petrenko, G. Balakrishnan, M. R. Lees, D. Mck. Paul and A. Hoser, *Phys. Rev. B: Condens. Matter*, 2000, **62**, 8983.

18 B. Bernu, C. Lhuillier and L. Pierre, *Phys. Rev. Lett.*, 1992, **69**, 2590.

19 L. Capriotti, A. E. Trumper and S. Sorella, *Phys. Rev. Lett.*, 1999, **82**, 3899.

20 G. Misguich, C. Lhuillier, B. Bernu and C. Waldtmann, *Phys. Rev. B: Condens. Matter*, 1999, **60**, 1064.

21 W. LiMing, G. Misguich, P. Sindzingre and C. Lhuillier, *Phys. Rev. B: Condens. Matter*, 2000, **62**, 6372.

22 M. Hemmida, H.-A. Krug von Nidda, N. Büttgen, A. Loidl, L. K. Alexander, R. Nath, A. V. Mahajan, R. F. Berger, R. J. Cava, Y. Singh and D. C. Johnston, *Phys. Rev. B: Condens. Matter Mater. Phys.*, 2009, **80**, 054406.

23 M. Hemmida, H.-A. Krug von Nidda and A. Loidl, *J. Phys. Soc. Jpn.*, 2011, **80**, 053707.

24 J. M. Kosterlitz and D. J. Thouless, *J. Phys. Chem.*, 1973, **6**, 1181.

25 J. M. Kosterlitz, *J. Phys. Chem.*, 1974, **7**, 1046.

26 V. L. Berezinskii, *Sov. Phys. JETP*, 1971, **32**, 493.

27 V. L. Berezinskii, *Sov. Phys. JETP*, 1972, **34**, 610.

28 O. A. Smirnova, V. B. Nalbandyan, A. A. Petrenko and M. Avdeev, *J. Solid State Chem.*, 2005, **178**, 1165.

29 M. A. Evstigneeva, V. B. Nalbandyan, A. A. Petrenko, B. S. Medvedev and A. A. Kataev, *Chem. Mater.*, 2011, **23**, 1174.

30 E. A. Zvereva, M. A. Evstigneeva, V. B. Nalbandyan, O. A. Savelieva, S. A. Ibragimov, O. S. Volkova, L. I. Medvedeva, A. N. Vasiliev, R. Klingeler and B. Büchner, *Dalton Trans.*, 2012, **41**, 572.

31 L. Viciu, Q. Huang, E. Morosan, H. W. Zandbergen, N. I. Greenbaum, T. McQueen and R. J. Cava, *J. Solid State Chem.*, 2007, **180**, 1060.

32 S. Derakhshan, H. L. Cuthbert, J. E. Greedan, B. Rahaman and T. Saha-Dasgupta, *Phys. Rev. B: Condens. Matter Mater. Phys.*, 2007, **76**, 104403.

33 Y. Miura, R. Hirai, T. Fujita, Y. Kobayashi and M. Sato, *J. Magn. Magn. Mater.*, 2007, **310**, 389.

34 Y. Miura, Y. Yasui, T. Moyoshi, M. Sato and K. Kakurai, *J. Phys. Soc. Jpn.*, 2008, **77**, 104709.

35 Y. Singh and P. Gegenwart, *Phys. Rev. B: Condens. Matter Mater. Phys.*, 2010, **82**, 064412.

36 V. V. Politaev and V. B. Nalbandyan, *Solid State Sci.*, 2009, **11**, 144.

37 V. V. Politaev, V. B. Nalbandyan, A. A. Petrenko, I. L. Shukaev, V. A. Volotchaev and B. S. Medvedev, *J. Solid State Chem.*, 2010, **183**, 684.

38 C. N. Kuo, T. S. Jian and C. S. Lue, *J. Alloys Compd.*, 2012, **531**, 1.

39 A. C. Larson and R. B. Von Dreele, *LAUR 86-748*, Los Alamos National Laboratory, Los Alamos, NM, 2004.

40 B. H. Toby, *J. Appl. Crystallogr.*, 2001, **34**, 210.

41 M. E. Matsnev and V. S. Rusakov, SpectrRelax – an application for Mössbauer spectra modeling and fitting, in *Abstract Book of Int. Conf. on Mössbauer Spectroscopy and its Applications*, Ekaterenburg, 2009, p. 181.

42 A. I. Popa, E. Vavilova, C. Täschner, V. Kataev, B. Büchner and R. Klingeler, *J. Phys. Chem. C*, 2011, **115**, 5265.

43 C. Golze, A. Alfonsov, R. Klingeler, B. Büchner, V. Kataev, C. Mennerich, H.-H. Klauss, M. Goiran, J.-M. Broto, H. Rakoto, S. Demeshko, G. Leibeling and F. Meyer, *Phys. Rev. B: Condens. Matter Mater. Phys.*, 2006, **73**, 224403.

44 F. Menil, *J. Phys. Chem. Solids*, 1985, **46**, 763.

45 *Mössbauer Spectroscopy*, ed. D. P. E. Dickson and F. J. Berry, Cambridge University Press, 1986.

46 F. van der Woude and G. A. Sawatzky, *Phys. Rev. B: Solid State*, 1971, **4**, 3159.

47 V. M. Buznik, *Glass Phys. Chem.*, 2000, **26**, 1.

48 Y. Sakurai, H. Arai and J. Yamaki, *Solid State Ionics*, 1998, **115**, 29.

49 A. K. Padhi, K. S. Nanjundaswamy and J. B. Goodenough, *J. Electrochem. Soc.*, 1997, **144**, 1188.

50 G. A. Bain and J. F. Berry, *J. Chem. Educ.*, 2008, **85**, 532.

51 R. Leidl, R. Klingeler, B. Büchner, M. Holtschneider and W. Selke, *Phys. Rev. B: Condens. Matter Mater. Phys.*, 2006, **73**, 224415.

52 A. Tari, *The specific heat of matter at low temperature*, Imperial College Press, London, 2003.

53 L. J. de Jongh and A. R. Miedema, *Adv. Phys.*, 1974, **23**, 1.

54 R. L. Carlin, *Magnetochemistry*, Springer-Verlag, Berlin Heidelberg New York Tokyo, 1986.

55 D. V. West, T. M. McQueen, I. D. Posen, X. Ke, Q. Huang, H. W. Zandbergen, A. J. Williams, P. Schiffer and R. J. Cava, *J. Solid State Chem.*, 2009, **182**, 1343.

56 Y. Tanaka, H. Tanaka, T. Ono, A. Oosawa, K. Morishita, K. Iio, T. Kato, H. Aruga Katori, M. I. Bartashevich and T. Goto, *J. Phys. Soc. Jpn.*, 2001, **70**, 3068.

57 V. A. Ivanshin, J. Deisenhofer, H.-A. Krug von Nidda, A. Loidl, A. Mukhin, J. Balbashov and M. V. Eremin, *Phys. Rev. B: Condens. Matter*, 2000, **61**, 6213.

58 A. Abragam and B. Bleaney, *Electron paramagnetic resonance of transition ions*, Clarendon Press, Oxford, 1970.

59 W. Low, *Paramagnetic Resonance of Solids*, Academic Press Inc., New York, 1960.

60 C. M. Brodbeck and R. R. Bukrey, *Phys. Rev. B*, 1981, **24**, 2334.

61 K. Kawasaki, *Prog. Theor. Phys.*, 1968, **39**, 285; K. Kawasaki, *Phys. Lett. A*, 1968, **26**, 543.

62 H. Mori and K. Kawasaki, *Prog. Theor. Phys.*, 1962, **28**, 971.

63 D. L. Huber, *Phys. Rev. B: Solid State*, 1972, **6**, 3180.

64 J. Kuriata, L. Sadlowski, B. Bojanowski, J. Walczak, M. Kurzawa and J. Pichet, *Phys. Status Solidi A*, 1988, **109**, K139.

65 J. Walczak, M. Kurzawa, J. Kuriata and L. Sadlowski, *Phys. Status Solidi B*, 1985, **132**, K99.

66 E. Dormann and V. Jaccarino, *Phys. Lett. A*, 1974, **48**, 81.

67 P. Gaveau, J. P. Boucher, L. P. Regnault and Y. Henry, *J. Appl. Phys.*, 1991, **69**, 6228.

68 L. P. Regnault, J. Rossat-Mignod, J. Y. Henry and L. P. De Jongh, *J. Magn. Magn. Mater.*, 1983, **31**, 1205.

69 M. Heinrich, H.-A. Krug von Nidda, A. Loidl, N. Rogado and R. J. Cava, *Phys. Rev. Lett.*, 2003, **91**, 137601.

70 K. Okuda, K. Kurosawa, Sh. Saito, M. Honda, Zh. Yu and M. Date, *J. Phys. Soc. Jpn.*, 1986, **55**, 4456.

71 H. Kawamura and S. J. Miyashita, *J. Phys. Soc. Jpn.*, 1984, **53**, 4138.

72 T. Okubo and H. Kawamura, *J. Phys. Soc. Jpn.*, 2010, **79**, 084706.

73 H. Kawamura, A. Yamamoto and T. Okubo, *J. Phys. Soc. Jpn.*, 2010, **79**, 023701.

74 A. P. Young, *Phys. Rev. B*, 1979, **19**, 1855.

75 A. Cuccoli, T. Roscilde, R. Vaia and P. Verrucchi, *Phys. Rev. Lett.*, 2003, **90**, 167205.

76 A. Cuccoli, T. Roscilde, V. Tognetti, R. Vaia and P. Verrucchi, *Phys. Rev. B*, 2003, **67**, 104414.